Assessment of radiation dose in nuclear cardiovascular imaging using realistic computational models

Tianwu Xie
Division of Nuclear Medicine and Molecular Imaging, Geneva University Hospital, Geneva 4 CH-1211, Switzerland

Choonsik Lee
Division of Cancer Epidemiology and Genetics, National Cancer Institute, National Institute of Health, Bethesda, Maryland 20852

Wesley E. Bolch
Departments of Nuclear & Radiological and Biomedical Engineering, University of Florida, Gainesville, Florida 32611

Habib Zaidi[a)]
Division of Nuclear Medicine and Molecular Imaging, Geneva University Hospital, Geneva 4 CH-1211, Switzerland; Geneva Neuroscience Center, Geneva University, Geneva CH-1205, Switzerland; and Department of Nuclear Medicine and Molecular Imaging, University of Groningen, University Medical Center Groningen, Groningen 9700 RB, Netherlands

(Received 4 December 2014; revised 24 April 2015; accepted for publication 8 May 2015; published 21 May 2015)

Purpose: Nuclear cardiology plays an important role in clinical assessment and has enormous impact on the management of a variety of cardiovascular diseases. Pediatric patients at different age groups are exposed to a spectrum of radiation dose levels and associated cancer risks different from those of adults in diagnostic nuclear medicine procedures. Therefore, comprehensive radiation dosimetry evaluations for commonly used myocardial perfusion imaging (MPI) and viability radiotracers in target population (children and adults) at different age groups are highly desired.
Methods: Using Monte Carlo calculations and biological effects of ionizing radiation VII model, we calculate the *S*-values for a number of radionuclides (Tl-201, Tc-99m, I-123, C-11, N-13, O-15, F-18, and Rb-82) and estimate the absorbed dose and effective dose for 12 MPI radiotracers in computational models including the newborn, 1-, 5-, 10-, 15-yr-old, and adult male and female computational phantoms.
Results: For most organs, ^{201}Tl produces the highest absorbed dose whereas ^{82}Rb and ^{15}O-water produce the lowest absorbed dose. For the newborn baby and adult patient, the effective dose of ^{82}Rb is 48% and 77% lower than that of ^{99m}Tc-tetrofosmin (rest), respectively.
Conclusions: ^{82}Rb results in lower effective dose in adults compared to ^{99m}Tc-labeled tracers. However, this advantage is less apparent in children. The produced dosimetric databases for various radiotracers used in cardiovascular imaging, using new generation of computational models, can be used for risk-benefit assessment of a spectrum of patient population in clinical nuclear cardiology practice.
 [http://dx.doi.org/10.1118/1.4921364]

Key words: radiation dosimetry, SPECT, PET, cardiovascular imaging, Monte Carlo

1. INTRODUCTION

Nuclear cardiovascular imaging plays a pivotal role in the assessment of myocardial ischemia, infarction, and damage associated with various congenital or acquired heart diseases.[1] Each year, more than 10×10^6 nuclear cardiac studies are performed in the US for the assessment of myocardial perfusion and/or viability.[2] These procedures are performed using a variety of either single-photon-emitting (SPECT) or positron-emitting (PET) radiotracers, involving the exposure of patients to radiation ranging between 5 and 57 mSv.[2] The growth of nuclear cardiology studies led to substantial increase of radiation dose to patients, placing them as major contributors to global radiological burden, actually accounting for 85% of nuclear medicine exposure to the US population.[3] In pediatric cardiology, myocardial perfusion imaging (MPI) is used in cardiac stress tests of children,[4] monitoring of myocardial ischemia,[5] evaluation of the effects of coronary arterial intervention,[6] stratification of cardiac risks of children with Kawasaki disease,[7] detection of congenital heart disease,[8] identification of myocardial perfusion in children after arterial switch operation,[9] estimation of right ventricular pressure overload,[10] and determination of myocardial disease (such as hypertrophic cardiomyopathy and cardiomyopathy in Duchenne muscular dystrophy).[11] However, the exposure of pediatric patients to ionizing radiation during nuclear cardiology procedures is a matter of concern.[12,13] With the same absolute level of radiation dose, children may experience greater stochastic effects from ionizing radiation than adults because they have a proportionally higher percentage of

TABLE I. Organ masses of computational phantoms.

		Newborn		1-yr-old		5-yr-old		10-yr-old		15-yr-old		Adult	
Organs\masses (g)	ID	Female	Male	Female	Male	Female	Male	Female	Male	Female	Male	Female	Male
Adipose tissue	11	658.7	659.3	3653.0	3652.6	4642.8	4649.0	6 435.8	6 435.8	11 649.8	6 748.7	23 632.0	20 350.1
Adrenal	12	5.9	5.9	4.0	4.0	5.0	5.0	7.0	7.0	9.0	10.0	13.0	14.0
Brain	13	314.8	314.8	945.2	945.2	1241.0	1241.0	1 305.4	1 305.4	1 294.0	1 415.5	1 301.1	1 450.5
Colon wall	14	16.8	16.8	49.4	49.4	118.4	118.4	206.9	206.8	295.6	297.8	360.0	369.9
Colon content	15	43.8	43.8	50.8	50.8	89.7	89.7	93.6	93.6	158.8	243.7	320.0	300.1
GB wall	16	0.5	0.5	1.4	1.4	2.6	2.6	4.4	4.4	7.2	7.5	10.2	13.9
GB content	17	2.8	2.8	8.0	8.0	14.9	14.9	25.8	25.8	41.5	44.7	45.8	54.1
Heart wall	18	19.9	19.9	50.0	50.0	85.2	85.2	138.3	138.3	219.7	229.9	250.5	329.9
Heart content	19	6.0	6.0	47.4	47.4	133.6	133.6	228.3	228.3	317.6	425.2	370.0	510.0
Kidney cortex	20	18.3	18.3	51.0	51.0	79.4	79.4	131.3	131.3	176.2	183.2	192.5	217.0
Kidney medulla	21	6.5	6.5	18.2	18.2	28.8	28.8	46.8	46.8	62.1	65.2	68.8	77.6
Kidney pelvis	22	1.3	1.3	3.5	3.5	5.6	5.6	9.1	9.1	12.0	12.8	13.8	15.5
Liver	23	128.6	128.6	327.1	327.1	567.0	567.0	824.5	824.5	1 290.5	1 290.4	1 400.0	1 799.8
Lung	24	58.8	58.8	149.3	149.3	297.9	297.9	489.1	489.1	752.9	886.8	950.3	1 201.5
Pancreas	25	6.0	6.0	19.8	19.8	34.6	34.6	59.7	59.7	99.2	109.1	120.0	140.0
Salivary glands	26	5.9	5.9	23.7	23.7	33.6	33.6	43.9	43.9	62.7	67.0	70.0	85.0
SI wall	27	29.3	29.3	82.1	82.1	210.9	210.9	355.6	357.5	496.4	503.3	601.1	649.9
SI content	28	31.4	31.4	48.9	48.9	38.3	38.3	162.6	161.6	279.1	267.3	280.9	350.0
Spinal cord	29	6.4	6.4	24.6	24.6	31.4	31.4	68.5	68.5	68.4	42.5	18.6	36.6
Spleen	30	9.4	9.4	28.7	28.7	49.6	49.6	79.4	79.4	128.9	128.7	130.0	150.0
Stomach wall	31	6.9	6.9	19.7	19.7	49.5	49.5	83.7	83.7	118.5	117.5	140.0	150.0
Stomach content	32	25.0	25.0	66.1	66.1	82.7	82.7	116.3	116.3	199.4	199.8	230.0	250.0
Thymus	33	12.8	12.8	16.1	16.1	30.0	30.0	37.5	37.5	29.9	34.6	20.0	25.0
Thyroid	34	1.3	1.3	1.8	1.8	3.4	3.4	7.8	7.8	12.1	11.9	17.0	20.0
UB wall	35	3.9	3.9	8.8	8.9	15.7	15.6	24.3	24.8	34.3	39.4	40.0	50.0
UB content	36	9.9	9.9	9.9	10.9	60.7	60.7	97.4	97.0	132.2	151.0	199.2	200.0
Blood vessel	37	11.0	11.0	23.6	23.6	62.3	62.3	134.0	134.0	226.1	252.5	384.3	371.5
Muscle	38	1530.0	1532.8	3186.8	3155.3	7367.7	7364.3	16 285.3	16 288.4	26 141.4	34 689.0	17 500.0	28 971.7
Cortical bone	39	76.4	76.4	293.3	293.3	735.7	735.7	1 704.6	1 704.6	2 932.7	3 264.6	3 228.0	4 438.4
Spongiosa	40	171.2	171.2	572.8	572.8	1266.7	1266.7	2 668.8	2 668.8	4 047.8	4 674.5	3 919.3	5 906.0
Ovaries[a]/testes[b]	41	0.3	0.8	0.8	1.5	2.0	1.7	3.4	2.0	5.8	15.8	11.0	35.0
Uterus[a]/prostate[b]	42	3.9	0.8	1.5	1.0	3.0	1.2	4.0	1.6	29.6	4.3	80.0	17.0
Cartilage	43	126.1	126.1	37.7	37.7	55.9	55.9	128.2	128.2	150.7	138.8	651.7	145.2
Penis[b]/ureter[c]	44	—	0.6	—	3.6	—	6.5	—	6.6	—	29.2	15.0	16.0
Pituitary gland	45	0.1	0.1	0.2	0.2	0.3	0.3	0.4	0.4	0.5	0.5	0.6	0.6
Tonsil	46	0.1	0.1	0.5	0.5	2.0	2.0	2.9	2.9	2.9	2.9	3.0	3.0
Breast	47	0.1	0.1	0.4	0.4	0.9	0.9	7.6	7.6	306.7	14.7	500.1	25.0
Esophagus	48	2.0	2.0	4.9	4.9	9.9	9.9	17.8	17.8	27.9	29.4	35.0	40.0
Bronchi	49	0.4	0.4	2.0	2.0	3.0	3.0	3.6	3.5	7.3	8.0	8.7	66.3
Eye balls	50	5.9	5.9	6.8	6.8	10.8	10.8	11.7	11.7	13.0	12.9	14.6	14.6
Larynx	51	1.3	1.3	3.9	3.9	6.8	6.8	11.8	11.8	14.4	21.7	14.3	28.4
Lens	52	0.1	0.1	0.2	0.2	0.3	0.3	0.4	0.4	0.4	0.5	0.4	0.4
Nasal layer	53	0.8	0.8	2.1	2.1	8.5	8.5	9.0	9.0	9.0	11.5	4.3	11.0
Oral cavity layer	54	0.7	0.7	0.6	0.6	1.2	1.2	1.1	1.1	8.0	5.2	22.5	35.8
Pharynx[d]/lymphatic nodes[c]	55	0.3	0.3	0.8	0.8	1.9	1.9	1.9	1.9	3.1	2.9	79.4	138.1
Tongue	56	3.5	3.5	9.8	9.8	18.8	18.8	31.5	31.5	52.8	55.4	41.6	42.3
Trachea	57	0.5	0.5	1.5	1.5	2.4	2.4	4.4	4.4	5.4	7.5	8.0	10.0
Skin	58	96.5	98.2	188.0	211.8	638.2	642.8	806.4	809.7	1 690.1	1 806.7	2 749.9	3 882.0
Total body[e] (kg)	100	3.5	3.5	10.0	10.0	18.2	18.2	32.9	32.9	53.6	58.6	60.1	73.0
Height[e] (cm)	—	47.0	47.0	77.0	77.0	110.0	110.0	140.0	140.0	161.0	166.0	163.0	176.0

[a]Organ for female.
[b]Organ for male.
[c]Organ for pediatric phantoms.
[d]Organ for adult phantoms.
[e]The height for the 1-yr, 5-yr, and 10-yr-old phantoms and the weight of all phantoms were chosen according to the reference data provided in the ICRP publication 89, while the height for the newborn and 15-yr-old phantoms was obtained from the NHANES IV (1999–2002) survey.

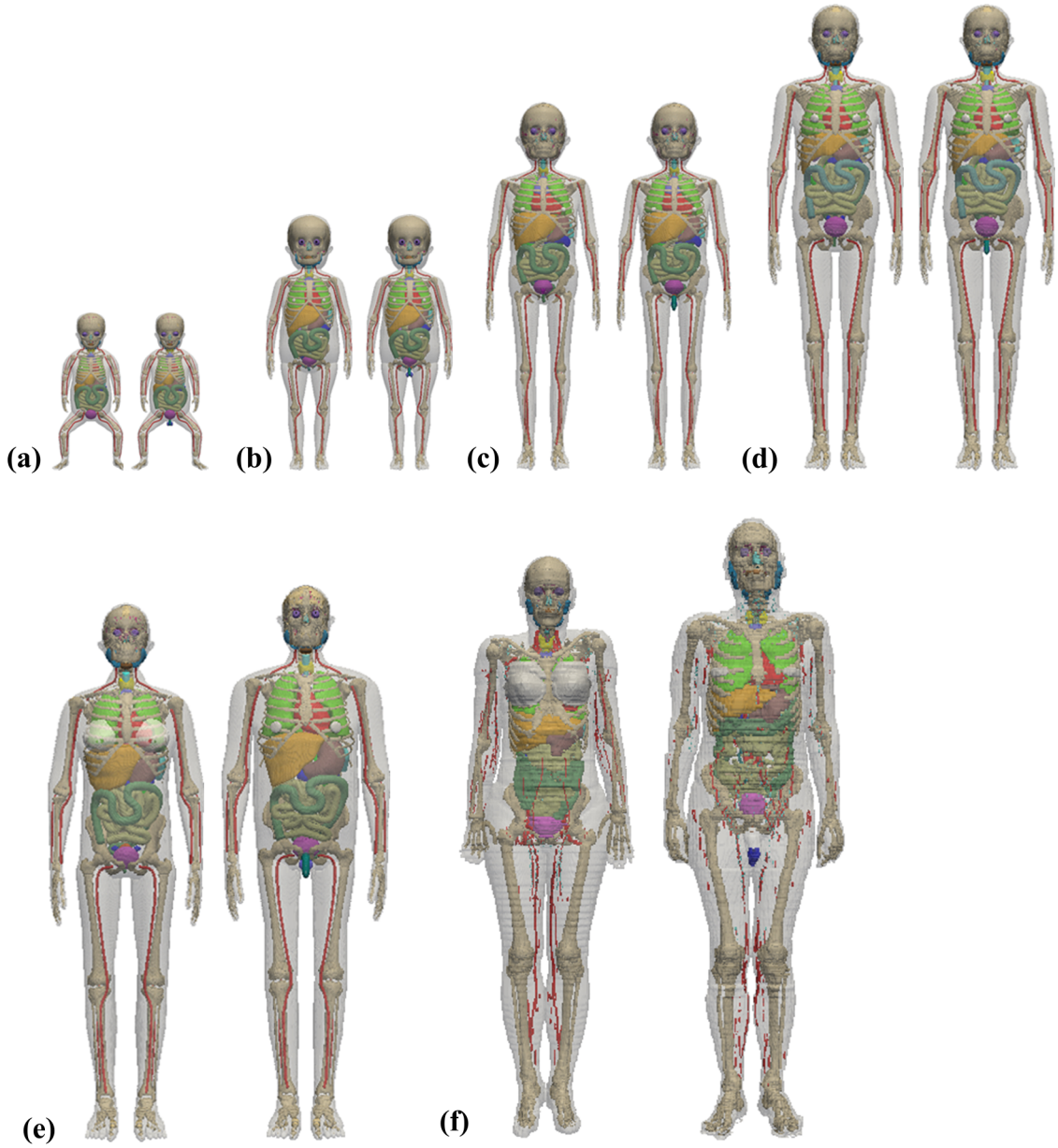

FIG. 1. 3D visualization of computational phantoms of (a) newborn, (b) 1-yr-old, (c) 5-yr-old, (d) 10-yr-old, (e) 15-yr-old, and (f) adult male (right) and female (left).

replicating cells, which are more radiosensitive than other cells.[14] Since children have longer postirradiation life period for the emergence of deleterious stochastic effects, they are also at higher cancer risk from ionizing radiation compared to adults.[15] Therefore, the assessment of absorbed radiation dose for patient populations of various age groups resulting from nuclear cardiology imaging procedures (SPECT and PET) is of paramount importance in clinical practice.

To this end, organ absorbed doses are often estimated using computational phantoms and Monte Carlo calculations.[16–22] These phantoms and computer codes, respectively, mimic the morphology and internal anatomic structures of the human body and simulate the interaction of ionizing radiation with biological tissues, thus allowing tracking the transport of radiation in the body. Depending on their geometric features, computational models can be divided into three basic categories: stylized models which employ simple equation-based mathematical functions, voxel-based models which use matrices obtained from segmented medical images, and boundary representation (BREP) models which employ nonuniform rational B-splines (NURBS) or polygonal meshes to represent the surface contour of individual organs and the whole body.[23–26] In most studies reported in the literature, the estimation of organ absorbed dose for a spectrum of populations of different ages from radiopharmaceuticals used in nuclear cardiology was performed using mathematical phantoms,[27–29] MIRDOSE (Ref. 30), or OLINDA/EXM version 1.0.[31] The new version of the latter, OLINDA/EXM version 2.0,[32] replaced the previous generation of mathematical phantoms with realistic NURBS-based anthropomorphic models, thus providing more accurate dose calculations. Significant differences were reported between dosimetric results of stylized and

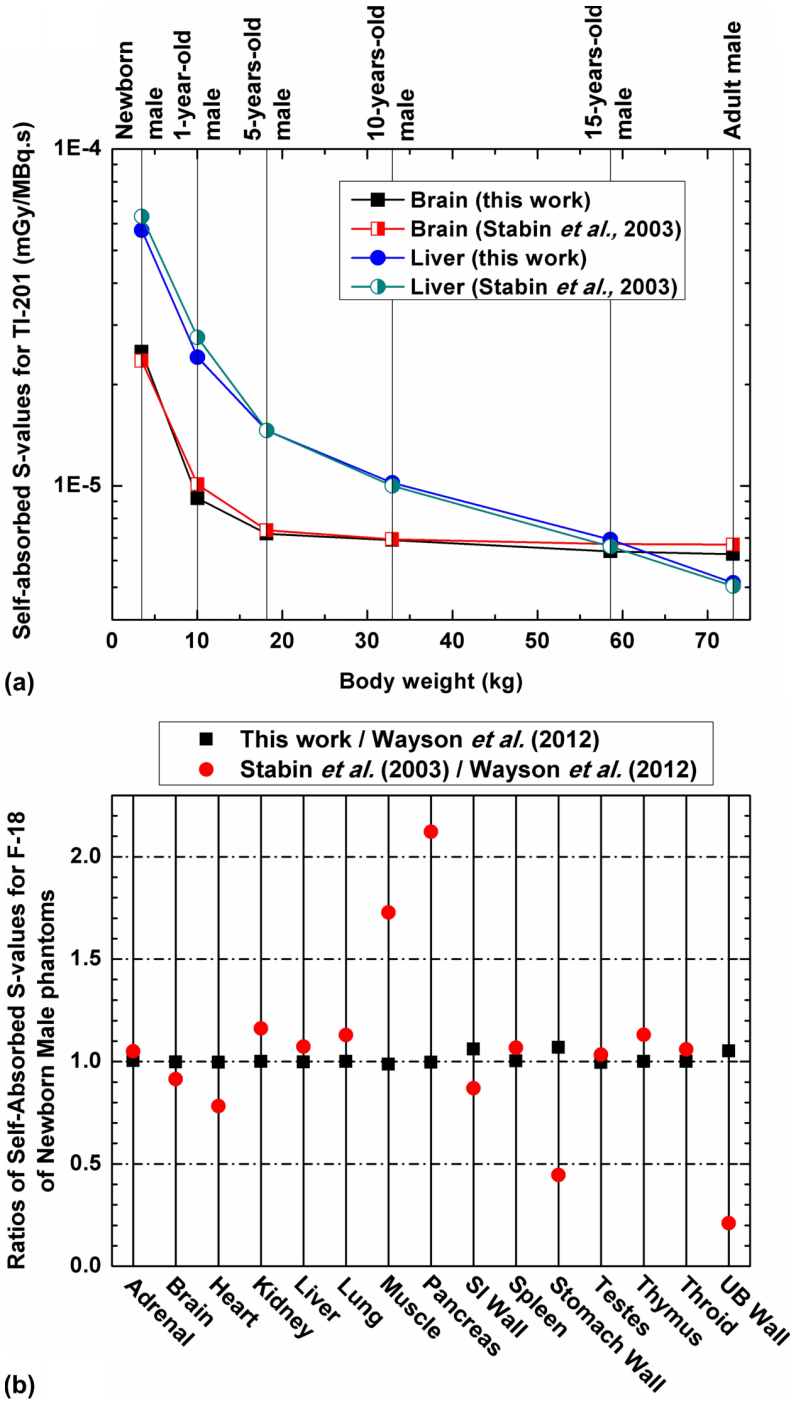

FIG. 2. (a) Comparisons of self-absorbed absorbed S-values for ^{201}Tl of the brain and liver between the results of this work and Stabin and Siegel (Ref. 57) for male. (b) Comparisons of self-absorbed S-values of the newborn male phantom obtained in this work and reported by Stabin and Siegel (Ref. 57) to those reported by Wayson *et al.* (Ref. 58) for F-18.

voxel-based models of the same subject.[33–39] For a variety of exposure conditions, the differences of effective dose between stylized adult phantom and voxel-based adult phantom of ICRP reference anatomic data have been reported to range between −50% and 60%.[40] For pediatric populations, the relative differences of the effective dose between University of Florida-National Cancer Institute (UF-NCI) phantoms and stylized phantoms may change between −24% and 33% for positron-emitting radiotracers.[35] Therefore, the assessment of organ absorbed dose and effective dose for commonly used nuclear cardiology radiotracers using new generation computational phantoms is desired.

In this work, we use the UF-NCI family of pediatric models and the ICRP reference adult voxel-based phantom to perform Monte Carlo-based particle transport simulation of radiation emitted by different radionuclides (Tl-201, Tc-99m, I-123, C-11, N-13, O-15, F-18, and Rb-82) to calculate S-values for the considered series of anatomical models. The obtained radiation dosimetry database is then used for the assessment of organ absorbed doses and effective dose of 12 radiotracers

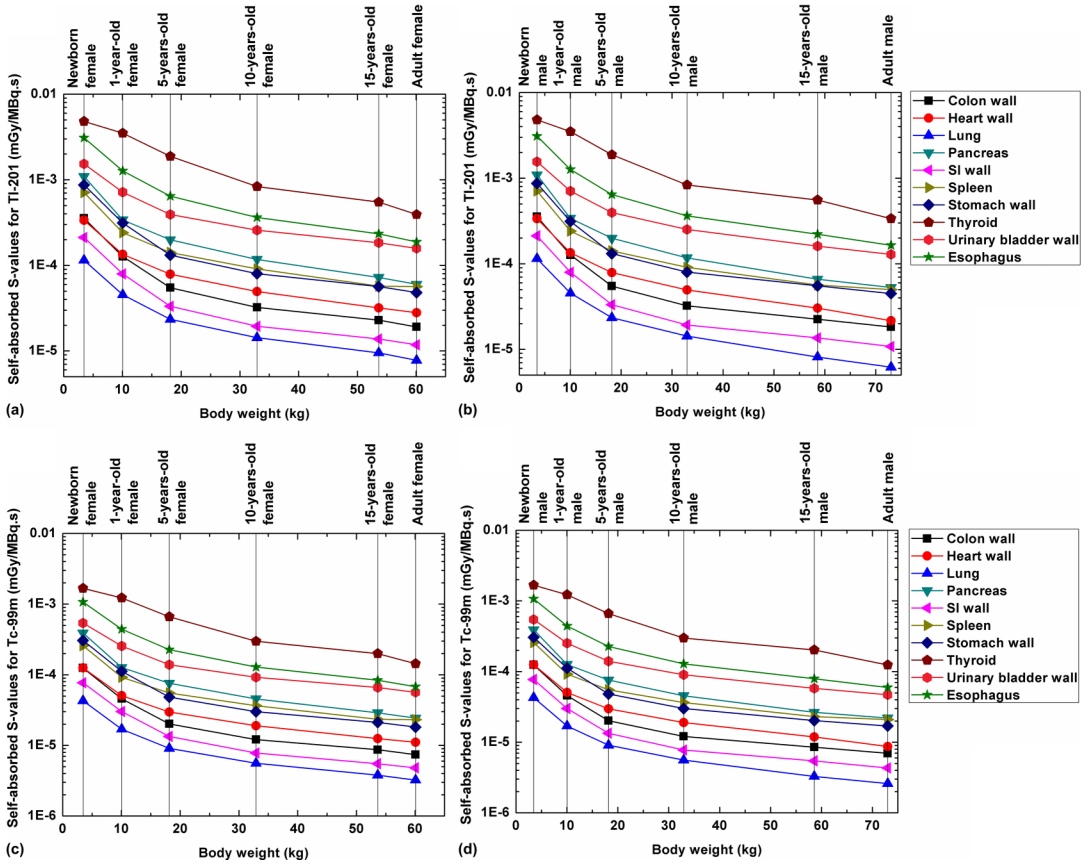

FIG. 3. Comparisons of self-absorbed S-values for selected internal organs of ^{201}Tl in (a) female and (b) male and ^{99m}Tc in (c) female and (d) male.

used in nuclear cardiac imaging. The effective dose per unit administered activity of 12 radiotracers was calculated for the newborn, 1-, 5-, 10-, 15-yr-old, and adult population based on the new ICRP tissue-weighting factors. Understanding the variability of the absorbed dose with patient's body weight and age may advance the perception of the uncertainties involved in internal radiation dosimetry calculations and risk-benefit analyses in pediatric nuclear cardiology practice. The detailed age-specific dosimetric calculations can be used for both prospective monitoring of cumulative exposure to chronic patients requiring multiple diagnostic procedures, as well as retrospective epidemiological studies.

2. MATERIALS AND METHODS

2.A. Computational phantoms

The UF-NCI hybrid pediatric phantom series were developed from patients' CT images using 3D image segmentation software and Rhinoceros package. The modeled NURBS-based UF-NCI phantoms were voxelized using an in-house MATLAB code. For the alimentary tract organs of the UF-NIC phantoms, the central trace of each segment was first extracted from original patient CT images and adjusted to match corresponding ICRP reference lengths. A NURBS pipe model was then generated along the constructed central tracks until a realistic shape and curvature were obtained. The thicknesses of the alimentary tract wall were modified to match corresponding ICRP reference masses. The voxelized UF-NCI computational phantom series, including the reference newborn, 1-, 5-, 10-, and 15-yr-old male and female models, and the ICRP reference adult male and female phantoms, were used in this work to represent patient populations of various ages for Monte Carlo-based internal radiation dosimetry calculations. The organ masses and body weights of the UF-NCI phantoms and ICRP reference models are close to the recommended anatomical data reported by the ICRP for population of corresponding age groups.[41,42] A unified voxel dimension of $1.8\times1.8\times3$ mm^3 was set for all computational models (interpolated from the original resolution) to minimize the differences across different models. For the sake of convenience in terms of effective dose calculation, homogeneous organs such as the left lung and right lung, the submaxillary salivary gland and sublingual salivary gland, the cartilage, cortical bone, and spongiosa at different bone sites were merged as one identified region. A unified organ ID was set for the UF-NCI phantom series and ICRP models. Body weights and organ/tissue masses for the pediatric and adult phantoms are summarized in Table I. Figure 1 shows the front 3D views of the 12 computational phantoms used in this work.

2.B. Monte Carlo simulations

The Monte Carlo N-particle extended—MCNPX—code (version 2.5.c) was adopted for radiation transport simulation in the UF-NCI and ICRP reference phantoms. The decay data of the investigated radionuclides were obtained from the radiation dose assessment resource (RADAR).[43] Uniformly

distributed radionuclide sources (Tl-201, Tc-99m, I-123, C-11, N-13, O-15, F-18, and Rb-82) were simulated in 48 source regions. The energy spectrum of photons, positrons, and electrons were determined from the decay schemes of the investigated isotopes and were manually defined in MCNPX input file. See supplementary Table A15 for decay data of the investigated radionuclides.[61] The energy deposition in the target regions was recorded in unit of MeV per particle using the MCNPX tally card *F8. The MCPLIB02 photon cross section library and the default electron/positron transport algorithms of MCNP were adopted for radiation transport simulations. An in-house c++ code was developed to process the output of the MCNP code and calculate the *S*-values of radionuclides as well as the absorbed doses and effective doses for the considered radiotracers using published biokinetic data from various sources[28,29,44,45] and the tissue weight factors recommended by ICRP publication 103.[46] The density and elemental compositions of organs/tissues for each anatomical model were obtained from the reference data reported in ICRP publication 89.[42] A total of 1.0×10^7 primary particles were generated such that the statistical uncertainty in terms of coefficient of variation was less than 2% in most cases.

2.C. Cardiovascular imaging radiotracers

The radiotracers investigated in this work are ^{201}Tl, ^{99m}Tc-sestamibi, ^{99m}Tc-tetrofosmin, ^{99m}Tc-furifosmin, ^{123}I-BMIPP, ^{11}C (realistic maximum model), ^{13}N-ammonia, ^{15}O-water, ^{18}F-flurpiridaz, ^{18}F-FDG, ^{18}F-LMI1195, and ^{82}Rb. Of these tracers, ^{201}Tl has been extensively used as a perfusion radiotracer in cardiovascular imaging owing to its excellent myocardial first pass extraction and good relationship between blood flow and myocardial uptake at higher flow rates during stress testing.[47] ^{99m}Tc-sestamibi, ^{99m}Tc-tetrofosmin, and ^{99m}Tc-furifosmin have experienced widespread sustained clinical use in nuclear cardiology since the 1990s,[48,49] whereas ^{123}I-BMIPP proved to be a useful iodinated branch chain fatty acid for evaluation of myocardial fatty acid uptake.[50,51] ^{11}C-labeled radiotracers, such as ^{11}C-*meta*-hydroxyephedrine, are adopted for PET imaging of heart failure.[52] ^{13}N-ammonia, ^{15}O-water, ^{82}Rb, and ^{18}F-FDG are common PET tracers and are increasingly used for myocardial perfusion and viability studies because of advantages they offer in terms of improved diagnostic accuracy and functional assessments.[53] ^{18}F-LMI1195 is a novel ^{18}F-labeled ligand for the norepinephrine transporter for mapping cardiac nerve terminals[54] whereas ^{18}F-flurpiridaz is a novel PET mitochondrial complex 1 inhibitor for detection of coronary artery disease and risk stratification.[55] The biokinetic data of these radiotracers were obtained from the supplementary materials of ICRP publication 80,[28] ICRP publication 106 (Ref. 29), and the additional literature.[44,45]

2.D. Dosimetry calculations

S-values of Tl-201, Tc-99m, I-123, C-11, N-13, O-15, F-18, and Rb-82 as well as the absorbed dose and effective dose

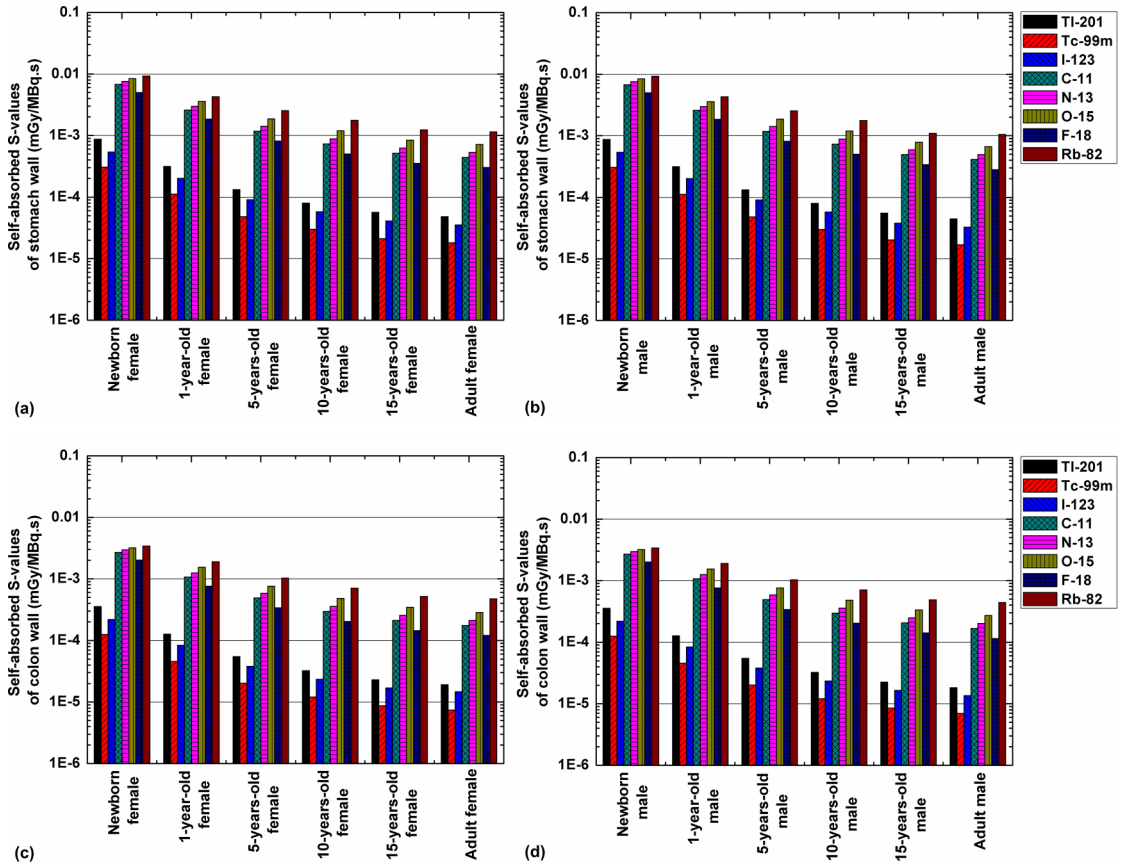

FIG. 4. Comparisons of self-absorbed *S*-values of radionuclides of ^{201}Tl, ^{99m}Tc, ^{123}I, ^{11}C, ^{13}N, ^{15}O, ^{18}F, and ^{82}Rb for the stomach wall of (a) female and (b) male and colon wall of (c) female and (d) male.

of 12 nuclear cardiology radiotracers were calculated for the newborn, 1-, 5-, 10-, 15-yr-old, and the adult male and female computational phantoms according to the medical internal radiation dose (MIRD) schema.[56] The radiation absorbed dose $D(r_T,T_D)$ delivered to any target tissue r_T from source organ r_S is given by

$$D(r_T,T_D) = \sum_{r_S} \tilde{A}(r_S,T_D) S(r_T \leftarrow r_S), \quad (1)$$

where $\tilde{A}(r_S,T_D)$ is the cumulated (time-integrated) activity of the radiopharmaceutical in the source region and $S(r_T \leftarrow r_S)$ is the S-value describing the equivalent dose rate in the target organ per unit activity in the source organ. The latter can be calculated by $S(r_T \leftarrow r_S) = 1/M_T \sum_i E_i Y_i \phi(r_T \leftarrow r_S, E_i)$, where E_i is the individual energy of the ith radiation, Y_i is the yield of ith radiation per nuclear transformation, M_T is the mass of the target organ, $\phi(r_T \leftarrow r_S, E_i)$ is the absorbed fraction given by $\phi(r_T \leftarrow r_S, E_i) = E_d/E_i$, where E_d is the recorded energy deposition in the target tissue. The uncertainty estimation of S-values for isotope R in target organ r_T is given by $S_R = 1/M_T \sqrt{\sum_i (Y_i F_i \bar{x}_i)^2}$ where F_i and $\bar{x}_i$ are output relative errors and scored values by MCNP tallies for the ith radiation in the considered target regions, respectively.

The equivalent dose, which relates the absorbed dose to stochastic effects, is calculated by multiplying the absorbed dose of organs by the radiation-weighting factors. To reflect the combined detriment from stochastic effects of equivalent doses in all organs of the human body, the concept of effective dose was introduced by the ICRP and is calculated by the sum of the product of tissue-weighting factor (ω_T) and equivalent doses.[46] The effective dose is defined by a weighted sum of tissue equivalent doses as Effective dose $= \sum_T \omega_T H_{r_T} = \sum_T \omega_T \sum_R \omega_R D_R(r_T,T_D)$, where ω_T is the tissue-weighting factors for target organ r_T, ω_R is the radiation-weighting factor for radiation type R, and H_{r_T} is the absorbed equivalent dose in the target organ from the administered radiotracer.

3. RESULTS

3.A. *S*-values

The S-values of eight investigated radionuclides for the considered source-target organ pairs were calculated in the considered computational phantoms. Figure 2 illustrates the self-absorbed S-values of Tl-201 for the brain and liver of the newborn, 1-, 5-, 10-, 15-yr-old, and adult male phantoms and the self-absorbed S-values of F-18 for representative organs of the male newborn. Comparisons between the results obtained in this work and those reported by Stabin and Siegel[57] and Wayson *et al.*[58] for self-absorbed S-values are shown. The same trend can be seen in Fig. 2(a) for self-absorbed S-values of Tl-201 for the brain and liver between

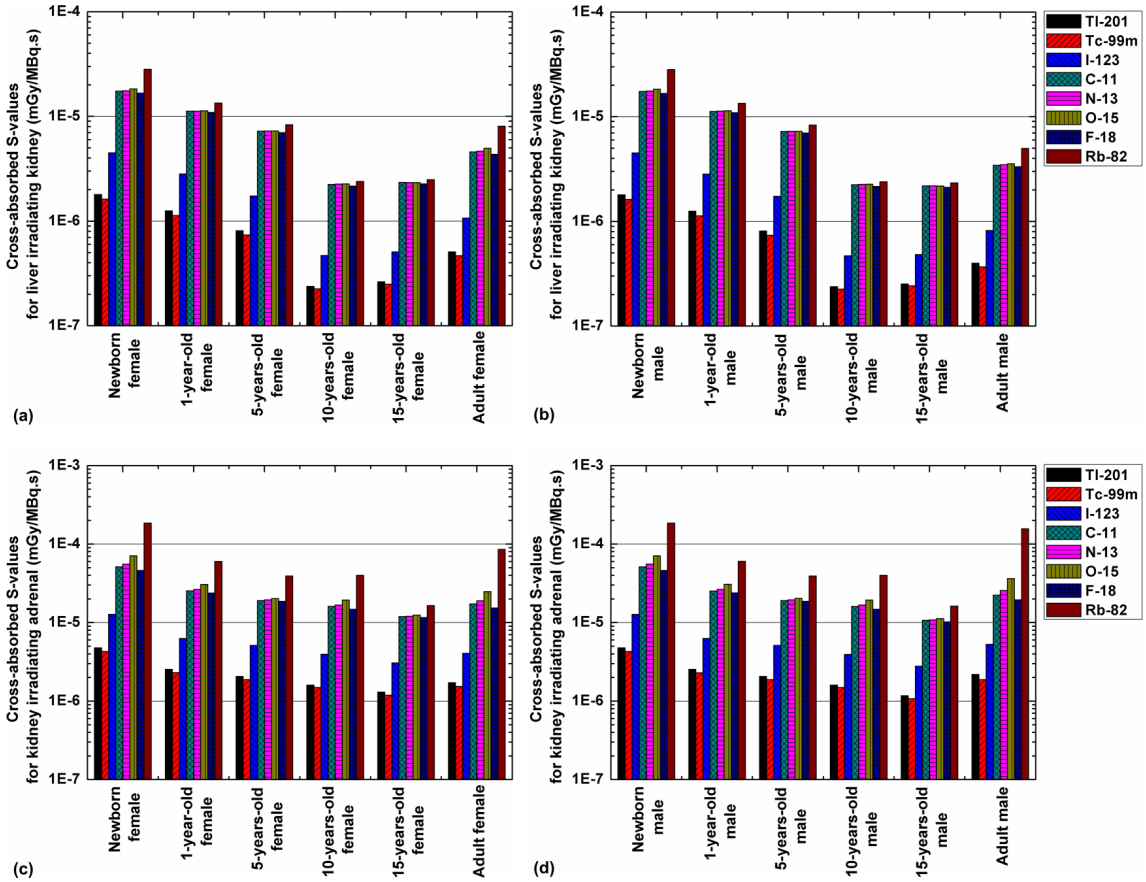

FIG. 5. Comparisons of cross-absorbed S-values of radionuclides of ^{201}Tl, ^{99m}Tc, ^{123}I, ^{11}C, ^{13}N, ^{15}O, ^{18}F, and ^{82}Rb for liver irradiating kidney of (a) female and (b) male models and kidney irradiating adrenal of (c) female and (d) male models.

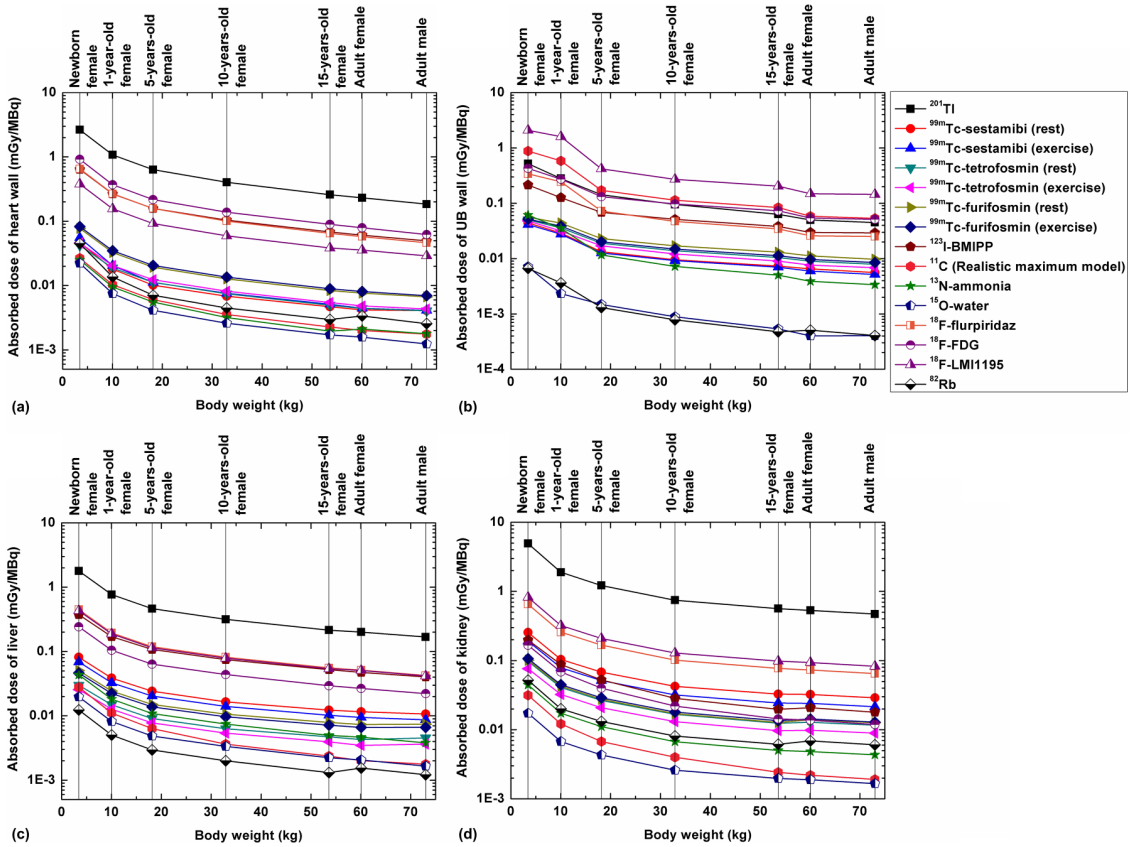

FIG. 6. Comparisons of absorbed dose of (a) heart wall, (b) UB wall, (c) liver and, (d) kidney from investigated 14 radiotracers.

our results and those reported in the literature for population of different age groups. For solid organs of the newborn phantom [Fig. 2(b)], there is good agreement between *S*-values of self-irradiation scenarios between this work and Wayson *et al.*[58] while for hollow organs, the self-absorbed *S*-values of organ walls are about 5%–7% larger than those of Wayson *et al.*[58] and present a higher sensitivity to changes in the voxel size ($0.663\times0.663\times0.663$ mm^3 for the model used by Wayson *et al.*[58] and $1.8\times1.8\times3$ mm^3 for the model used in this work). The *S*-value differences between the results of Stabin and Siegel[57] and this work may be attributed to the differences between the geometries of the stylized and voxel-based models.

Figure 3 shows the self-absorbed *S*-values of Tl-201 and Tc-99m for selected internal organs. For all radionuclides, the self-absorbed *S*-values of organs decrease when the body weight increases and present with negative correlations with organ mass. The correlation between the cross-absorbed *S*-values and body weight is more complicated because the energy deposition pattern of particles in the target region from cross-irradiation is more affected by source/target distance.

Figures 4 and 5 illustrate the self-absorbed *S*-values for the stomach wall and colon wall and the cross-absorbed *S*-values for the liver irradiating the kidney and the kidney irradiating the adrenals, respectively, for the defined computational phantoms and the eight considered radionuclides. Of these radionuclides, Rb-82 and Tc-99m produce the largest and lowest self-absorbed *S*-values for most organs, respectively. For SPECT radionuclides, the self-absorbed organ *S*-values for Tl-201 and I-123 are quite similar and about 70%–190% larger than those obtained for Tc-99m, while the cross-absorbed organ *S*-values for Tl-201 and Tc-99m are comparable and about 50%–60% smaller than those obtained for I-123. The cross-absorbed *S*-values of C-11, N-13, O-15, and F-18 are similar and about 9 times higher than those of Tl-201 and Tc-99m. A plausible explanation of these observations is that the cross-absorbed *S*-values are mostly contributed by photons[38] and the 511 keV annihilation photons emitted by positron-emitting radionuclides contribute similar energy deposition patterns and result in higher energy deposition in target regions than the low-energy photons emitted by Tl-201 and Tc-99m.

3.B. Absorbed dose and effective dose

The absorbed dose to 48 target organs from the 12 investigated radiotracers was calculated in the considered computational phantoms. It was observed that the highest absorbed dose to critical organs is delivered to the testes, kidney, thyroid, and heart wall for ^{201}Tl; gall bladder wall, kidney, salivary glands, liver, uterus, colon wall, and urinary bladder wall for ^{99m}Tc-sestamibi, ^{99m}Tc-tetrofosmin, and ^{99m}Tc-furifosmin; heart wall, liver, and urinary bladder wall for ^{123}I-BMIPP; the UB wall and uterus for ^{11}C (realistic maximum model); the liver, urinary bladder wall, and kidney for ^{13}N-ammonia; the liver, spleen, thyroid, and testes for ^{15}O-water; the kidney, heart wall, and liver for

^{18}F-flurpiridaz; the heart wall and urinary bladder wall for ^{18}F-FDG; the urinary bladder wall and thyroid for ^{18}F-LMI1195; and uterus, kidney, and lung for ^{82}Rb. Figure 6 shows the absorbed dose from considered radiotracers for the heart wall, UB wall, kidney, and liver for the newborn, 1-, 5-, 10-, 15-yr-old female, and the adult male and female models. For the kidney, the absorbed dose from ^{201}Tl is about 300, 90, and 20 times higher than from ^{15}O-water, ^{82}Rb, and ^{99m}Tc-sestamibi (rest), respectively. For most radiotracers, the organ absorbed dose per unit administered activity decreases when the body weight increases. Among all considered radiotracers, ^{201}Tl produces the highest absorbed dose to all organs because of the long half-life of the radionuclide (73 h), in contrast to the relatively shorter half-lives of ^{15}O-water and ^{82}Rb (2.04 and 1.27 min), respectively, which produces the lowest absorbed dose in most organs. However, for the UB wall, ^{18}F-LMI1195 produces the highest absorbed dose because of its long residence time in the urinary bladder. Figure 7 shows the absorbed dose per unit administered activity to representative critical organs of ^{99m}Tc-sestamibi, ^{99m}Tc-tetrofosmin, ^{18}F-flurpiridaz, and ^{82}Rb. For most organs, organ absorbed doses in the newborn phantom are 3.6–8.5 times higher than those of 10-yr-old phantom and 7.6–13.1 times higher than those of the adult for the considered radiotracers.

The effective dose per unit administered activity of 12 radiotracers in the newborn, 1-, 5-, 10-, 15-yr-old, and adult models calculated using tissue-weighting factors of the ICRP 103 is shown in Fig. 8. Among the considered radiotracers and population of various age groups, ^{201}Tl produces the highest effective dose ranging from 0.099 to 1.49 mSv/MBq, while ^{15}O-water and ^{82}Rb produce the lowest effective dose ranging from 0.001 to 0.014 mSv/MBq and 0.001 to 0.021 mSv/MBq, respectively. Tc-99m-labeled radiotracers resulted in similar effective dose ranging from 0.004 to 0.054 mSv/MBq. The effective doses of ^{123}I-BMIPP, ^{18}F-flurpiridaz, and ^{18}F-FDG are comparable and about 86% lower than those of ^{201}Tl and 4.4 times and 14 times higher than the effective dose of Tc-99m-labeled tracers and ^{82}Rb, respectively. The effective dose of ^{82}Rb is about 80% and 50% lower than the corresponding dose of Tc-99m-labeled tracers in the adult and the newborn, respectively. ^{18}F-LMI1195, as a novel investigational PET tracer for cardiovascular imaging, delivers a high absorbed dose to the urinary system (kidney and UB) and results in an effective dose ranging from 0.028 to 0.362 mSv/MBq to reference patients at different ages. See supplementary Tables A3–A14 for the calculated absorbed organ doses and effective doses for the considered radiotracers (the values are shown as mean value ±2 standard deviations).[61] The uncertainties associated with absorbed dose and effective dose estimates are computed directly from Monte Carlo estimates.

4. DISCUSSION

The voxel size of the ICRP reference male and female phantoms was interpolated from $2.137\times2.137\times8$ mm^3 and $1.775\times1.775\times4.84$ mm^3 to $1.8\times1.8\times3$ mm^3 with average

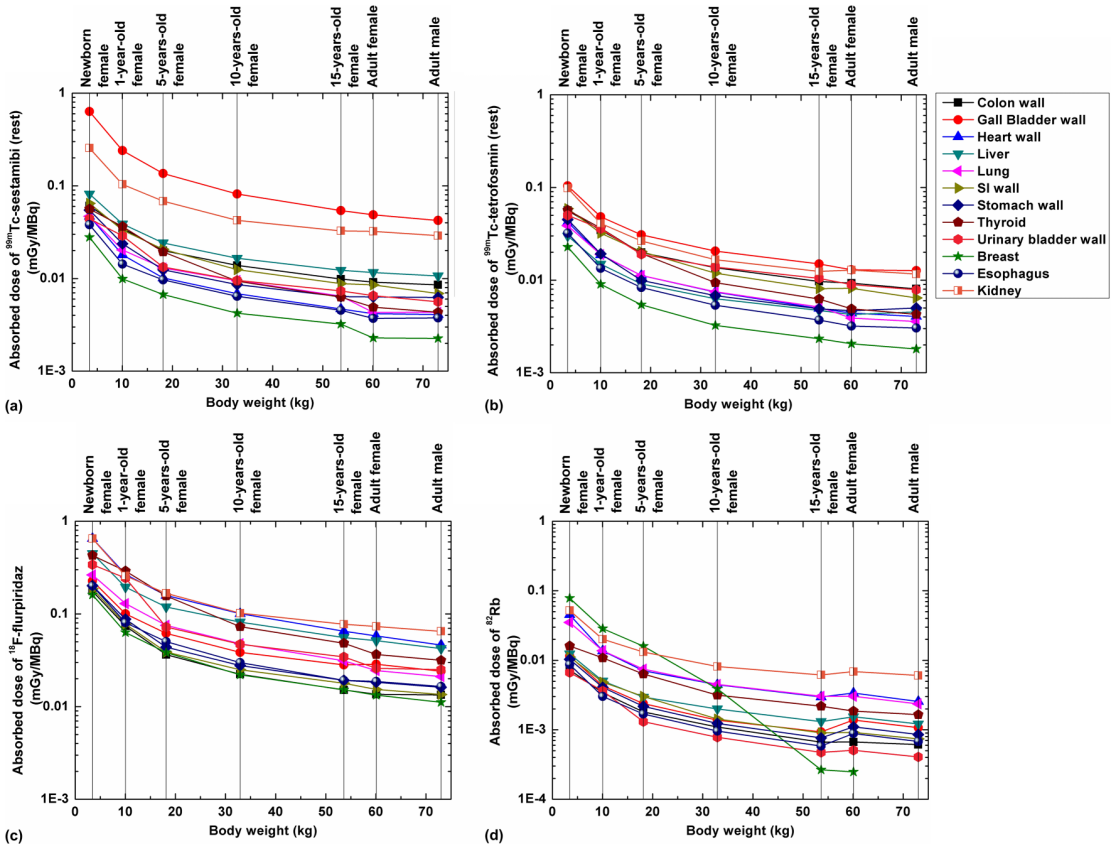

FIG. 7. Comparisons of absorbed dose for selected internal organs from (a) ^{99m}Tc-sestamibi (rest), (b) ^{99m}Tc-tetrofosmin (rest), (c) ^{18}F-flurpiridaz, and (b) ^{82}Rb.

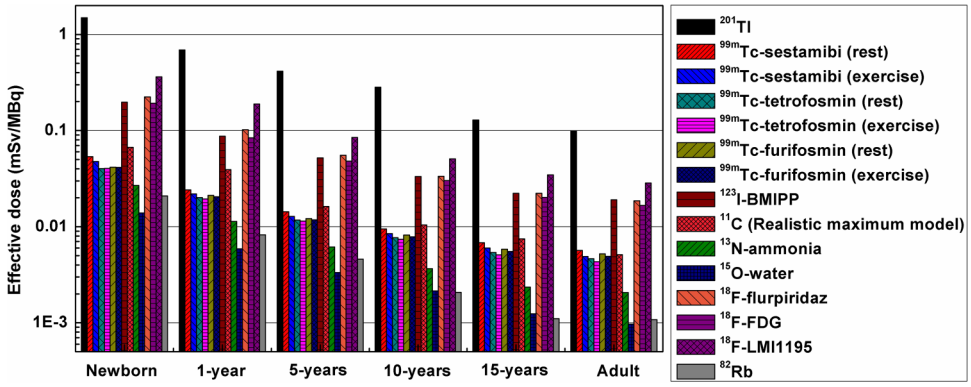

FIG. 8. Effective dose of 14 studied radiotracers of the newborn, 1-yr-old, 5-yr-old, 10-yr-old, 15-yr-old, and adult reference human.

interpolation errors of 0.07% and 0.13%, respectively. The largest errors introduced in organ volumes for the ICRP male and female phantoms were 1.99% and 1.43%, respectively. See supplementary Table A16 at Ref. 61 for tissue-weighting factors given in ICRP publication 103,[46] which are not age- and gender-specific and were used in this work for the calculation of the effective dose of both adult and pediatric phantoms. For children at different ages, the use of the effective dose calculated from recommended tissue-weighting factors may introduce uncertainties less than 40%.[59] Variability is also introduced when effective doses are calculated using different tissue-weighting factors. The mean relative difference between effective doses calculated using ICRP 60 and ICRP 103 tissue-weighting factors was reported to be about $7.3\% \pm 9.1\%$ for positron-emitting radiotracers using pediatric models.[35] The dose estimation in diagnostic nuclear medicine is commonly based on mean or median biokinetic data of a small group of animal or human subjects and the involved uncertainties have been reported to be within the range of 10%–30% for computational models (organs/tissues) of different sizes.[60]

The development of novel nuclear cardiology imaging probes for diagnosis of cardiovascular disease is an active research field.[53] Accurate dose calculations for representative patient groups at different ages are needed to optimize the dose regimens of various radiotracers and to investigate the collective radiation exposure and risks associated with nuclear medicine procedures. In this work, we estimated the *S*-values for Tl-201, Tc-99m, I-123, C-11, N-13, O-15, F-18, and Rb-82 using a new generation of age- and sex-dependent computational phantoms including the newborn, 1-, 5-, 10-, 15-yr-old, and adult male and female and calculated organ absorbed doses and effective doses of 12 radiotracers used in nuclear cardiology based on the latest available dosimetric data.

The Monte Carlo method is a powerful and popular tool for internal radiation dosimetry calculation where accurate dose estimates are grounded on reliable computational phantoms that mimic the internal anatomic geometries and physical characteristics of the human body. The equivalent dose to patients from administered radiotracers is frequently calculated from tabulated absorbed dose rate derived from stylized phantoms.[27–31] However, significant differences between the dosimetric characteristics of stylized and voxel-based models for the same subject are often reported.[33–38] Since some biological organs/tissues in populations of different ages may have substantially different physical and biochemical characteristics and present with different radiosensitivity and radiation risks, the evaluation of age-dependent absorbed dose using realistic anatomical computational phantoms is commended.

Among the evaluated radionuclides, Tl-201, Tc-99m, and I-123 are adopted for SPECT cardiovascular imaging while C-11, N-13, O-15, F-18, and Rb-82 are commonly used for PET cardiovascular imaging. The organ absorbed dose depends on the *S*-value and physical half-life of the radionuclide and the biological half-life and biodistribution of the radiotracer. For most organs, Rb-82 produces the highest self-absorbed *S*-values which decrease with increasing age and weight and the second lowest absorbed organ dose because of its short half-life. Overall, among the considered nuclear cardiology radiotracers, Tl-201-labeled tracers produce the highest absorbed dose and effective dose in humans; I-123 and F-18-labeled tracers produce the second highest radiation dose, while Tc-99m and C-11-labeled tracers produce the third highest radiation dose. A lower effective dose in adults is observed for ^{82}Rb-labeled tracers compared to ^{99m}Tc-labeled tracers, while this advantage is less apparent in children.

5. CONCLUSION

A systematic study was conducted to evaluate the radiation dose from nuclear cardiology (SPECT and PET) procedures to pediatric and adults populations using the latest generation computational phantoms and the up-to-date dosimetric data available. The generated database of organ absorbed dose and effective dose for radiotracers used in nuclear cardiovascular imaging can be used for radiation risk assessment for the pediatric and adult population in clinical routine.

ACKNOWLEDGMENTS

This work was supported by the Swiss National Science Foundation under Grant No. SNSF 31003A-149957 and Geneva Cancer League.

[a]Author to whom correspondence should be addressed. Electronic mail: habib.zaidi@hcuge.ch; Telephone: +41 22 372 7258; Fax: +41 22 372 7169.

[1]C. Kondo, "Myocardial perfusion imaging in pediatric cardiology," Ann. Nucl. Med. **18**, 551–561 (2004).
[2]E. Picano and E. Vano, "The radiation issue in cardiology: The time for action is now," Cardiovasc. Ultrasound **9**, 35–48 (2011).
[3]D. A. Schauer and O. W. Linton, "NCRP report no. 160, ionizing radiation exposure of the population of the United States, medical exposure-are we doing less with more, and is there a role for health physicists?," Health Phys. **97**, 1–5 (2009).
[4]Y. Ohmochi, Z. Onouchi, Y. Oda, and K. Hamaoka, "Assessment of effects of intravenous dipyridamole on regional myocardial perfusion in children with Kawasaki disease without angiographic evidence of coronary stenosis using positron emission tomography and H2(15)O," Coron. Artery Dis. **6**, 555–559 (1995); available at http://www.ncbi.nlm.nih.gov/pubmed/7582194.
[5]S. L. Jan, B. Hwang, Y. C. Fu, P. C. Lee, C. H. Kao, R. S. Liu, and C. S. Chi, "Comparison of 201Tl SPET and treadmill exercise testing in patients with Kawasaki disease," Nucl. Med. Commun. **21**, 431–435 (2000).
[6]C. Kondo, M. Hiroe, T. Nakanishi, and A. Takao, "Detection of coronary artery stenosis in children with Kawasaki disease. Usefulness of pharmacologic stress 201Tl myocardial tomography," Circulation **80**, 615–624 (1989).
[7]M. Miyagawa, T. Mochizuki, K. Murase, S. Tanada, J. Ikezoe, M. Sekiya, K. Hamamoto, S. Matsumoto, and M. Niino, "Prognostic value of dipyridamole-thallium myocardial scintigraphy in patients with Kawasaki disease," Circulation **98**, 990–996 (1998).
[8]H. Stern, U. Sauer, D. Locher, R. Bauer, H. Meisner, F. Sebening, and K. Buhlmeyer, "Left ventricular function assessed with echocardiography and myocardial perfusion assessed with scintigraphy under dipyridamole stress in pediatric patients after repair for anomalous origin of the left coronary artery from the pulmonary artery," J. Thorac. Cardiovasc. Surg. **106**, 723–732 (1993).
[9]A. M. Hayes, E. J. Baker, A. Kakadeker, J. M. Parsons, R. P. Martin, R. Radley-Smith, S. A. Qureshi, M. Yacoub, M. N. Maisey, and M. Tynan, "Influence of anatomic correction for transposition of the great arteries on myocardial perfusion: Radionuclide imaging with technetium-99m 2-methoxy isobutyl isonitrile," J. Am. Coll. Cardiol. **24**, 769–777 (1994).
[10]K. Nakajima, J. Taki, M. Taniguchi, N. Tonami, and K. Hisida, "Comparison of 99Tcm-sestamibi and 201Tl-chloride to estimate right ventricular overload in children," Nucl. Med. Commun. **16**, 936–941 (1995).
[11]T. Nishimura, A. Yanagisawa, H. Sakata, K. Sakata, K. Shimoyama, T. Ishihara, H. Yoshino, and K. Ishikawa, "Thallium-201 single photon emission computed tomography (SPECT) in patients with duchenne's progressive muscular dystrophy: A histopathologic correlation study," Jpn. Circ. J. **65**, 99–105 (2001).
[12]M. G. Stabin, "Radiopharmaceuticals for nuclear cardiology: Radiation dosimetry, uncertainties, and risk," J. Nucl. Med. **49**, 1555–1563 (2008).
[13]S. T. Treves, A. Baker, F. H. Fahey, X. Cao, R. T. Davis, L. A. Drubach, F. D. Grant, and K. Zukotynski, "Nuclear medicine in the first year of life," J. Nucl. Med. **52**, 905–925 (2011).
[14]E. Robbins, "Radiation risks from imaging studies in children with cancer," Pediatr. Blood Cancer **51**, 453–457 (2008).
[15]M. Steinert, M. Weiss, P. Gottlober, D. Belyi, O. Gergel, V. Bebeshko, N. Nadejina, I. Galstian, G. Wagemaker, T. M. Fliedner, and R. U. Peter, "Delayed effects of accidental cutaneous radiation exposure: Fifteen years of follow-up after the chernobyl accident," J. Am. Acad. Dermatol. **49**, 417–423 (2003).
[16]H. Zaidi and X. G. Xu, "Computational anthropomorphic models of the human anatomy: The path to realistic Monte Carlo modeling in medical imaging," Annu. Rev. Biomed. Eng. **9**, 471–500 (2007).
[17]X. G. Xu and K. F. Eckerman, "Computational phantoms for radiation dosimetry: A 40-year history of evolution," in *Handbook of Anatomical Models for Radiation Dosimetry* (Taylor & Francis, London, 2010), Chap. 1.
[18]M. G. Stabin and X. G. Xu, "Basic principles in the radiation dosimetry of nuclear medicine in radiation dosimetry and risk in the practice of nuclear medicine," Semin. Nucl. Med. **44**, 162–171 (2014).
[19]X. G. Xu, "An exponential growth of computational phantom research in radiation protection, imaging, and radiotherapy: A review of the fifty-year history," Phys. Med. Biol. **59**, R233–R302 (2014).
[20]Y. Liu, T. Xie, and Q. Liu, "Monte Carlo simulation for internal radiation dosimetry based on the high resolution visible Chinese human," Nucl. Sci. Tech. **22**, 165–173 (2011).
[21]W. Sun, X. Jia, T. Xie, F. Xu, and Q. Liu, "Construction of boundary-surface-based Chinese female astronaut computational phantom and proton dose estimation," J. Radiat. Res. **54**, 383–397 (2012).
[22]J. Ai, T. Xie, W. Sun, and Q. Liu, "Red bone marrow dose calculations in radiotherapy of prostate cancer based on the updated VCH adult male phantom," Phys. Med. Biol. **59**, 1815–1830 (2014).
[23]C. Lee, D. Lodwick, D. Hasenauer, J. L. Williams, C. Lee, and W. E. Bolch, "Hybrid computational phantoms of the male and female newborn patient: NURBS-based whole-body models," Phys. Med. Biol. **52**, 3309–3333 (2007).
[24]J. Zhang, Y. H. Na, P. F. Caracappa, and X. G. Xu, "RPI-AM and RPI-AF, a pair of mesh-based, size-adjustable adult male and female computational phantoms using ICRP-89 parameters and their calculations for organ doses from monoenergetic photon beams," Phys. Med. Biol. **54**, 5885–5908 (2009).
[25]C. H. Kim, J. H. Jeong, W. E. Bolch, K.-W. Cho, and S. B. Hwang, "A polygon-surface reference Korean male phantom (PSRK-Man) and its direct implementation in Geant4 Monte Carlo simulation," Phys. Med. Biol. **56**, 3137–3161 (2011).
[26]V. Cassola, V. de Melo Lima, R. Kramer, and H. Khoury, "FASH and MASH: Female and male adult human phantoms based on polygon mesh surfaces: I. Development of the anatomy," Phys. Med. Biol. **55**, 133–162 (2010).
[27]ICRP, "Publication 53: Radiation dose to patients from radiopharmaceuticals," Ann. ICRP **18**, 1–377 (1987).
[28]ICRP, "Publication 80: Radiation dose to patients from radiopharmaceuticals (addendum 2 to ICRP publication 53)," Ann. ICRP **28**, 1–126 (1998).
[29]ICRP, "Publication 106: Radiation dose to patients from radiopharmaceuticals. Addendum 3 to ICRP publication 53," Ann. ICRP **38**, 1–197 (2008).
[30]M. G. Stabin, "MIRDOSE: Personal computer software for internal dose assessment in nuclear medicine," J. Nucl. Med. **37**, 538–546 (1996).
[31]M. G. Stabin, R. B. Sparks, and E. Crowe, "OLINDA/EXM: The second-generation personal computer software for internal dose assessment in nuclear medicine," J. Nucl. Med. **46**, 1023–1027 (2005).
[32]M. Stabin and A. Farmer, "OLINDA/EXM 2.0: The new generation dosimetry modeling code," J. Nucl. Med. **53**, 585–586 (2012).
[33]N. Petoussi-Henss, M. Zankl, C. Hoeschen, and D. Nosske, "Voxel or MIRD-type model: A sensitivity study relevant to nuclear medicine," in *World Congress on Medical Physics and Biomedical Engineering 2006* (Springer, Berlin, 2007), Vol. 14, pp. 2061–2064.
[34]T. Xie, G. Zhang, Y. Li, and Q. Liu, "Comparison of absorbed fractions of electrons and photons using three kinds of computational phantoms of rat," Appl. Phys. Lett. **97**, 33702–33704 (2010).
[35]T. Xie and H. Zaidi, "Evaluation of radiation dose to anthropomorphic paediatric models from positron-emitting labelled tracers," Phys. Med. Biol. **59**, 1165–1187 (2014).
[36]T. Xie and H. Zaidi, "Fetal and maternal absorbed dose estimates for positron-emitting molecular imaging probes," J. Nucl. Med. **55**, 1459–1466 (2014).
[37]T. Xie and H. Zaidi, "Assessment of S-values in stylized and voxel-based rat models for positron-emitting radionuclides," Mol. Imaging Biol. **15**, 542–551 (2013).
[38]T. Xie, W. E. Bolch, C. Lee, and H. Zaidi, "Pediatric radiation dosimetry for positron-emitting radionuclides using anthropomorphic phantoms," Med. Phys. **40**, 102502 (13pp.) (2013).
[39]T. Xie and H. Zaidi, "Effect of respiratory motion on internal radiation dosimetry," Med. Phys. **41**, 112506 (10pp.) (2014).
[40]R. Kramer, H. Khoury, and J. Vieira, "Comparison between effective doses for voxel-based and stylized exposure models from photon and electron irradiation," Phys. Med. Biol. **50**, 5105–5126 (2005).
[41]C. Lee, J. L. Williams, C. Lee, and W. E. Bolch, "The UF series of tomographic computational phantoms of pediatric patients," Med. Phys. **32**, 3537–3548 (2005).
[42]ICRP, "Publication 89: Basic anatomical and physiological data for use in radiological protection: Reference values," Ann. ICRP **32**, 1–277 (2002).
[43]RADAR, http://www.doseinfo-radar.com/RADARDecay.html, 2014.
[44]J. Maddahi, J. Czernin, J. Lazewatsky, S. C. Huang, M. Dahlbom, H. Schelbert, R. Sparks, A. Ehlgen, P. Crane, Q. Zhu, M. Devine, and M. Phelps, "Phase I, first-in-human study of BMS747158, a novel 18F-labeled tracer for myocardial perfusion PET: Dosimetry, biodistribution, safety, and imaging characteristics after a single injection at rest," J. Nucl. Med. **52**, 1490–1498 (2011).

[45]S. Senthamizhchelvan, P. E. Bravo, C. Esaias, M. A. Lodge, J. Merrill, R. F. Hobbs, G. Sgouros, and F. M. Bengel, "Human biodistribution and radiation dosimetry of 82Rb," J. Nucl. Med. **51**, 1592–1599 (2010).
[46]ICRP, "Publication 103: The 2007 recommendations of the international commission on radiological protection," Ann. ICRP **37**, 1–332 (2007).
[47]W. Krahwinkel, H. Herzog, and L. E. Feinendegen, "Pharmacokinetics of thallium-201 in normal individuals after routine myocardial scintigraphy," J. Nucl. Med. **29**, 1582–1586 (1988).
[48]F. J. Wackers *et al.*, "Technetium-99m hexakis 2-methoxyisobutyl isonitrile: Human biodistribution, dosimetry, safety, and preliminary comparison to thallium-201 for myocardial perfusion imaging," J. Nucl. Med. **30**, 301–311 (1989).
[49]E. A. Platts, T. L. North, R. D. Pickett, and J. D. Kelly, "Mechanism of uptake of technetium-tetrofosmin. I: Uptake into isolated adult rat ventricular myocytes and subcellular localization," J. Nucl. Cardiol. **2**, 317–326 (1995).
[50]F. F. Knapp, Jr., M. M. Goodman, A. P. Callahan, and G. Kirsch, "Radioiodinated 15-(p-iodophenyl)-3,3-dimethylpentadecanoic acid: A useful new agent to evaluate myocardial fatty acid uptake," J. Nucl. Med. **27**, 521–531 (1986).
[51]Y. Fujibayashi, R. Nohara, R. Hosokawa, K. Okuda, Y. Yonekura, N. Tamaki, J. Konishi, S. Sasayama, and A. Yokoyama, "Metabolism and kinetics of iodine-123-BMIPP in canine myocardium," J. Nucl. Med. **37**, 757–761 (1996).
[52]R. K. Vesalainen, M. Pietila, K. U. Tahvanainen, T. Jartti, M. Teras, K. Nagren, P. Lehikoinen, R. Huupponen, H. Ukkonen, M. Saraste, J. Knuuti, and L. M. Voipio-Pulkki, "Cardiac positron emission tomography imaging with [11C]hydroxyephedrine, a specific tracer for sympathetic nerve endings, and its functional correlates in congestive heart failure," Am. J. Cardiol. **84**, 568–574 (1999).
[53]O. O. Sogbein, M. Pelletier-Galarneau, T. H. Schindler, L. Wei, R. G. Wells, and T. D. Ruddy, "New SPECT and PET radiopharmaceuticals for imaging cardiovascular disease," BioMed Res. Int. **2014**, 942960.
[54]A. J. Sinusas, J. Lazewatsky, J. Brunetti, G. Heller, A. Srivastava, Y. H. Liu, R. Sparks, A. Puretskiy, S. F. Lin, P. Crane, R. E. Carson, and L. V. Lee, "Biodistribution and radiation dosimetry of LMI1195: First-in-human study of a novel 18F-labeled tracer for imaging myocardial innervation," J. Nucl. Med. **55**, 1445–1451 (2014).
[55]M. Yu, S. G. Nekolla, M. Schwaiger, and S. P. Robinson, "The next generation of cardiac positron emission tomography imaging agents: Discovery of flurpiridaz F-18 for detection of coronary disease," Semin. Nucl. Med. **41**, 305–313 (2011).
[56]W. E. Bolch, K. F. Eckerman, G. Sgouros, and S. R. Thomas, "MIRD pamphlet no. 21: A generalized schema for radiopharmaceutical dosimetry–standardization of nomenclature," J. Nucl. Med. **50**, 477–484 (2009).
[57]M. G. Stabin and J. A. Siegel, "Physical models and dose factors for use in internal dose assessment," Health Phys. **85**, 294–310 (2003).
[58]M. Wayson, C. Lee, G. Sgouros, S. T. Treves, E. Frey, and W. E. Bolch, "Internal photon and electron dosimetry of the newborn patient—A hybrid computational phantom study," Phys. Med. Biol. **57**, 1433–1457 (2012).
[59]C. Martin, "Effective dose: How should it be applied to medical exposures?," Br. J. Radiol. **80**, 639–647 (2007).
[60]M. G. Stabin, "Uncertainties in internal dose calculations for radiopharmaceuticals," J. Nucl. Med. **49**, 853–860 (2008).
[61]See supplementary material at http://dx.doi.org/10.1118/1.4921364 for Tables A1–A16 cited in the text.